Selective Enhancement of Spectroscopic Features by Quantum Optimal Control

Daniel Keefer* and Shaul Mukamel†
Departments of Chemistry and Physics and Astronomy, University of California, Irvine, California 92697-2025, USA

(Received 26 January 2021; revised 12 March 2021; accepted 16 March 2021; published 19 April 2021)

Tailored light can be used to steer atomic motions into selected quantum pathways. In optimal control theory (OCT), the target is usually expressed in terms of the molecular wave function, a quantity that is not directly observable in experiment. We present simulations using OCT that optimize the spectroscopic signal itself. By shaping the optical pump, the x-ray stimulated Raman signal, which occurs solely during the passage through conical intersections, is temporally controlled and amplified by up to 2 orders of magnitude. This enhancement can be crucial in order to bring small coherence-based signatures above the detectable threshold. Our approach is applicable to any signal that depends on the expectation value of a positive definite operator.

DOI: 10.1103/PhysRevLett.126.163202

Interesting dynamical effects in molecules often show up as weak spectroscopic features. These are usually masked by stronger, less interesting contributions, making them hard to detect. Quantum optimal control [1,2] provides an effective tool that can be used to amplify desired parts of signals thus enabling their interpretation [3–6]. The underlying quantum pathways may be coherently manipulated by tailoring the spectral profile, timing, and polarization of the applied light fields [2]. Many successful examples of steering molecular photochemistry have been reported [7–11], and prominent applications of quantum control extend to a wide range of research areas like quantum computing [12,13], diamond-based quantum sensing [14], or coherent behavior in open quantum systems [1,15], to just name a few.

Here, we employ quantum optimal control theory (OCT) [16–18] to directly optimize spectroscopic observables. We demonstrate its capability on the transient redistribution of ultrafast electronic coherences in attosecond Raman signal (TRUECARS) that probes conical intersection dynamics via time-dependent distributions of vibronic coherences [19,20]. Initially demonstrated for a vibronic coupling model [19], recent simulations highlight its unique capabilities to detect nonadiabatic passages [20,21] in the RNA-nucleobase uracil. A few tens of femtoseconds after creating a nuclear wave packet in the bright S_2 electronic state, a conical intersection seam is reached. A vibronic coherence, i.e., wave packet overlap between S_2 and S_1, is created during the nonadiabatic passage. A hybrid broadband ε_0 narrowband ε_1 x-ray probe field is employed that transiently redistributes energy within the coherence by an off-resonant stimulated Raman process. The signal is given by

$$S(\omega,T)=2\mathcal{I}\int_{-\infty}^{\infty}dt e^{i\omega(t-T)}\varepsilon_0^*(\omega)\varepsilon_1(t-T)\times\langle\psi_a(t)|\hat{\alpha}_{ab}|\psi_b(t)\rangle. \quad (1)$$

Here T is the delay between the pump pulse and the detection, and ω is the Raman signal frequency shift with respect to the $\varepsilon_0(\omega)$ probe. The relevant material quantity is the time-dependent expectation value of the transition polarizability operator α_{ab} between two valence electronic states a and b that form a conical intersection. Although being free from the usually dominating population background, the stimulated Raman probing process must compete with loss channels like photoionization or Auger decay to record a sufficient number of photons on the detector. This is nontrivial, since coherences in molecular quantum dynamics (i.e., the overlap of the nuclear wave functions ψ_{ab} at two different electronic states) are usually weak. Additionally, far from any core resonance, the transition polarizability α_{ab} is weak as well. The signal strength is thus a crucial obstacle to experimental observation.

Our goal is to find the optimal pump laser pulse that controls the passage time through the conical intersection and maximizes the TRUECARS signal. We use the common Krotov's formulation of OCT [22] with strict limitations in the frequency domain [23]. In conventional OCT, the control target is expressed through the overlap of the molecular wave function $\psi(T)$ at time T with a desired target state Φ or via the projection of $\psi(T)$ onto a certain region on the potential energy surface [24,25]. However, the expectation value of any positive definite operator can be optimized instead [24,26]. We thus insert the time-dependent polarizability from Eq. (1) into the global control functional, which then reads [23,26]

$$J[\psi_i(t),\chi_f(t),\varepsilon_p] = \langle\psi_a(T)|\hat{\alpha}_{ab}|\psi_b(T)\rangle - \alpha_0\int_0^T \frac{|\varepsilon_p|^2}{s(t)}dt - \gamma|F[\varepsilon_p(t)]| - 2\mathcal{R}\left[\int_0^T \langle\chi_f(t)|\frac{i}{\hbar}(\hat{H}_0 - \hat{\mu}\varepsilon_p(t)) + \frac{\partial}{\partial t}|\psi_i(t)\rangle dt\right]. \quad (2)$$

This functional is expressed in terms of the initial time-dependent wave function $\psi_i(t)$, the electric field $\varepsilon_p(t)$ that governs it, and the Lagrange multiplier $\chi_f(t)$ that ensures satisfaction of the time-dependent Schrödinger equation in the fourth term. In the second term of Eq. (2), the Krotov change parameter α_0 penalizes high field intensities, $s(t)$ is a Gaussian function centered around $\varepsilon_p(t)$, ensuring a smooth switching on and off behavior of the electric field, and $F[\varepsilon_p(t)]$ is a filter operation with the Lagrange multiplier γ, which acts in the frequency domain of the pulse [23]. The fourth term in Eq. (2) governs the time-dependent Schrödinger equation with the unperturbed molecular Hamiltonian $\hat{H}_0$ and $\hat{\mu}$ is the dipole operator.

We employed our effective Hamiltonian for the photophysics of uracil [20,21,25]. It is based on *ab initio* electronic structure calculations involving two nuclear degrees of freedom q_1 and q_2 and three electronic states. Nuclear wave packet simulations are performed in this three-state two-mode Hamiltonian by solving the time-dependent Schrödinger equation on a numerical grid, yielding the complete nuclear + electronic wave function. Quantum effects of the nuclei that are important in the correct description of the light-matter interaction, and the nonadiabatic passage through the conical intersection, are exactly included. An optical 34 fs pump prepares the molecule in the bright S_2 state. In a corresponding experiment [27], an identical pump pulse (34 fs duration and 3×10^{11} W cm^{-2} peak intensity) has been used to initiate photodynamics in uracil. This was combined with a strong-field near-infrared probe pulse, which ionized the molecules with variable time delay. By detecting the ionization fragments with a time-of-flight mass spectrometer as a function of the pump-probe delay, few-femtosecond relaxation times were reported for the S_2 to S_1 transition, and the associated conical intersection has been identified by the supporting theory. Interestingly, adapting the ultraviolet pump parameters in our simulations leads to almost 100% population transfer from S_0 to S_2, while no statement about the fraction of excited molecules is made in Ref. [27].

After this initial step and a free evolution period in S_2, a conical intersection seam is reached. There, the wave packet relaxes to the S_1 state, giving rise to vibronic S_2/S_1 coherences and thus to the finite expectation value of the transition polarizability operator in Eq. (1) responsible for the TRUECARS signal. The excited state population dynamics and the polarizability are shown in Figs. 1(a) and 1(b). The transition polarizability operator in the two-dimensional nuclear space for a probe energy of 326 eV is depicted in Fig. 1(c). It has been calculated in the dipole approximation according to [28,29]

$$[\alpha_{xy}]_{ab} = \sum_c \left\{\frac{\langle a|\hat{\mu}_y|c\rangle\langle c|\hat{\mu}_x|b\rangle}{\omega_{ca}+\omega_0} + \frac{\langle a|\hat{\mu}_x|c\rangle\langle c|\hat{\mu}_y|b\rangle}{\omega_{cb}-\omega_0}\right\}, \quad (3)$$

where $\hat{\mu}_x$ and $\hat{\mu}_y$ are the Cartesian x and y components of the dipole operator in the molecular frame. The summation is over 80 off-resonant core-hole states c using the

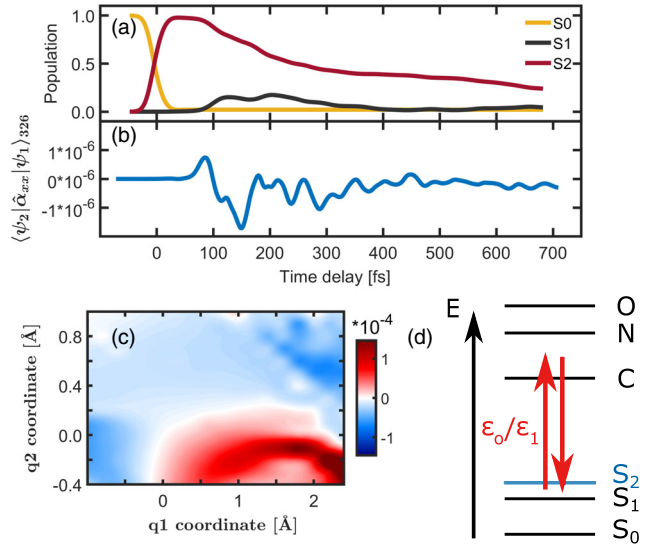

FIG. 1. Population dynamics and polarizability resulting from wave packet simulations in our effective uracil Hamiltonian [20,25]. The time delay is measured between the optical pump and the x-ray probe and is noted as T in Eq. (1). (a) A 34 fs optical pump [Fig. 3(a)] creates a population in the bright S_2 state. After a period of free wave packet evolution, a conical intersection seam is reached, and the wave packet decays into S_1, where it eventually absorbed. (b) Magnitude of the expectation value of the transition polarizability operator. Being initially zero, it becomes nonvanishing once the conical intersection is reached, and a vibronic coherence is created. (c) Off-resonant transition polarizability in the two-dimensional nuclear space of uracil at 326 eV probe energy, calculated by Eq. (3). The conical intersection seam is located at $q_1 = [1,2]$ and $q_2 = 0$ Å. (d) Level scheme of the experiment. A population is created in the bright S_2 state (blue) by the optical pulse ε_p. The x-ray fields ε_0 and ε_1 [compare Eq. (1)] probe the vibronic coherence between S_2 and S_1 via an off-resonant stimulated Raman process. C, N, and O are the carbon, nitrogen, and oxygen core states.

transition dipole moments between the final a and initial b valence state of the off-resonant Raman probing scheme. ω_{ca} and ω_{cb} are the transition energies, and ω_0 is the Raman probe frequency. The conical intersection seam is located between $q_1 = 1$–2 Å and $q_2 = 0$ Å and is visible in the polarizability due to change of electronic character along the conical intersection.

The goal is to tailor $\varepsilon_p(t)$ through iterative solution of Eq. (2) [24] in a way that maximizes $\langle\psi_a(T)|\hat{\alpha}_{ab}|\psi_b(T)\rangle$ in the x direction, which is within the molecular plane (further abbreviated $\langle\alpha_{xx}\rangle$) at time T. Although we only present results using this orientation here, pulses were optimized for each spatial direction separately, and all drawn conclusions can be made there as well. The control equations are solved according to the procedure outlined in Ref. [24]. The laser field profile in Fig. 3(a), corresponding to an unshaped excitation, was chosen as the guess field in the first iteration. A Krotov change parameter of $\alpha_0 = 1 \times 10^{-8}$ was used, along with a 30 fs full width at half maximum (FWHM) Gaussian shape function $s(t)$. Between 50 and 120 iterations were necessary to reach the optimal control fields.

As is evident from Fig. 1(b), the magnitude for an unshaped Gaussian pump excitation peaks between 80 and 200 fs, where the majority of the conical intersection passage takes place. Five final target times T were selected for the control simulations: 100, 120, 150, 175, and 200 fs. The polarizability in Fig. 1(c) with an x-ray probe energy of 326 eV was used for all simulations. $\langle\alpha_{xx}\rangle$ is shown in Fig. 2 for these five times. Our goal is clearly achieved: the magnitude of $\langle\alpha_{xx}\rangle$ is significantly amplified. Compared to the unshaped pulse results shown in Fig. 1(b), it occurs at the desired passage time.

Figure 3 depicts the optimized fields ε_p, their frequency-resolved optical gating (FROG) [30] spectrogram

$$I_{\mathrm{FROG}}(\omega, T) = \left| \int_{-\infty}^{\infty} dt \varepsilon_p(t) E_{\mathrm{gate}}(t - T) e^{-i\omega t} \right|^2, \quad (4)$$

as well as the TRUECARS signal [Eq. (1)]. Figure 3(a) depicts the unshaped 34 fs FWHM Gaussian laser pulse that has been used experimentally to photoexcite uracil [27]. Its spectrogram is simple, and the TRUECARS signal, in accordance with $\langle\alpha_{xx}\rangle$ in Fig. 1(b), is delocalized over several hundred femtoseconds. In contrast, Figs. 3(b)–3(f) show the optimized laser pulses that maximize $\langle\alpha_{xx}\rangle$ at different selected times. The signals are strongly amplified at the target time by up to 2 orders of magnitude compared to Fig. 1(a).

The optimal pulse spectrograms [Figs. 3(b)–3(f)] are significantly more complex, but within reach of current pulse shaping devices [31,32]. They cover a much broader frequency range than the unshaped pulse in Fig. 3(a). The main spectral contribution is often centered around the same wavelengths, with the exception of a slight redshift in Figs. 3(b) and 3(e) and a slight blueshift in Fig. 3(c). Additionally, the spectrograms in Figs. 3(b), 3(c), and 3(e) exhibit an up-chirp, i.e., the spectral contributions with higher frequency being delayed, whereas the spectrogram in Fig. 3(d) is slightly down-chirped. The maximum pulse intensities, polarizability magnitudes, and TRUECARS signal strengths are summarized in Table I. Starting from an intensity of 3×10^{11} W cm^{-2} for the unshaped Gaussian pulse, the shaped pulses exhibit intensities in the range of 10^{12}–10^{13} W cm^{-2}, where multiphoton processes can start to contribute. Practically, a trade-off between pulse intensity or complexity and the signal strength should be found. We tested for manual pulse simplification after the optimization by cutting out certain spectral contributions to the controlling laser pulses or by decreasing their peak intensity by factors of 2–10. In all cases, this comes at a cost of efficiency; i.e., the TRUECARS spectra were not as strong as in the optimal case, but still significantly stronger than the one generated with a truly unshaped pulse and shown in Fig. 3(a).

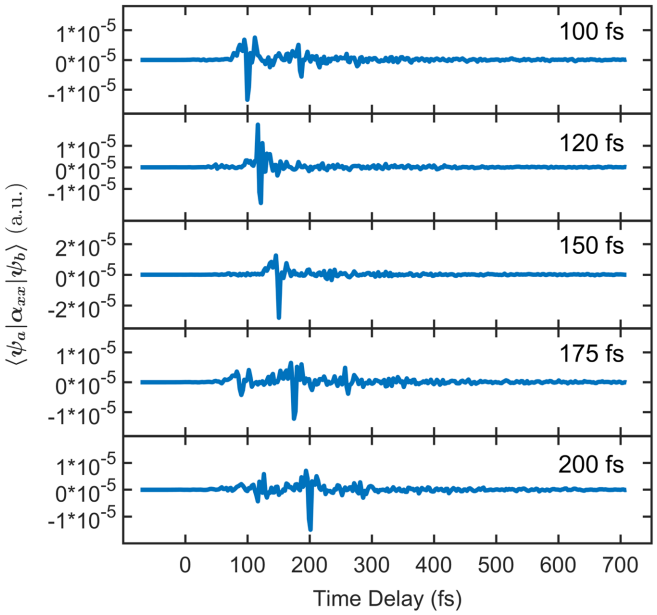

FIG. 2. The transition polarizability expectation value, which is the optimization target in Eq. (2), and the time-dependent material quantity in the TRUECARS signal [Eq. (1)] after pulse optimization. The time delay is measured between the optical pump and the x-ray probe and is denoted T in Eq. (1). Five different target times T in the nuclear dynamics were chosen at 100, 120, 150, 175, and 200 fs. Compared to Fig. 1(b), the magnitude has been amplified significantly, with the maximum value located at the target time.

An interesting aspect apparent from Table I is that the relative values of S_{max} and $\langle\alpha\rangle_{\mathrm{max}}$ vary between specific final times. In addition, their magnitudes at different times fluctuate between, e.g., $\langle\alpha\rangle_{\mathrm{max}} = 1.52 \times 10^{-5}$ at 175 fs and 2.80×10^{-5} at 150 fs. This has two reasons. First, the complex wave packet motion on the potential energy

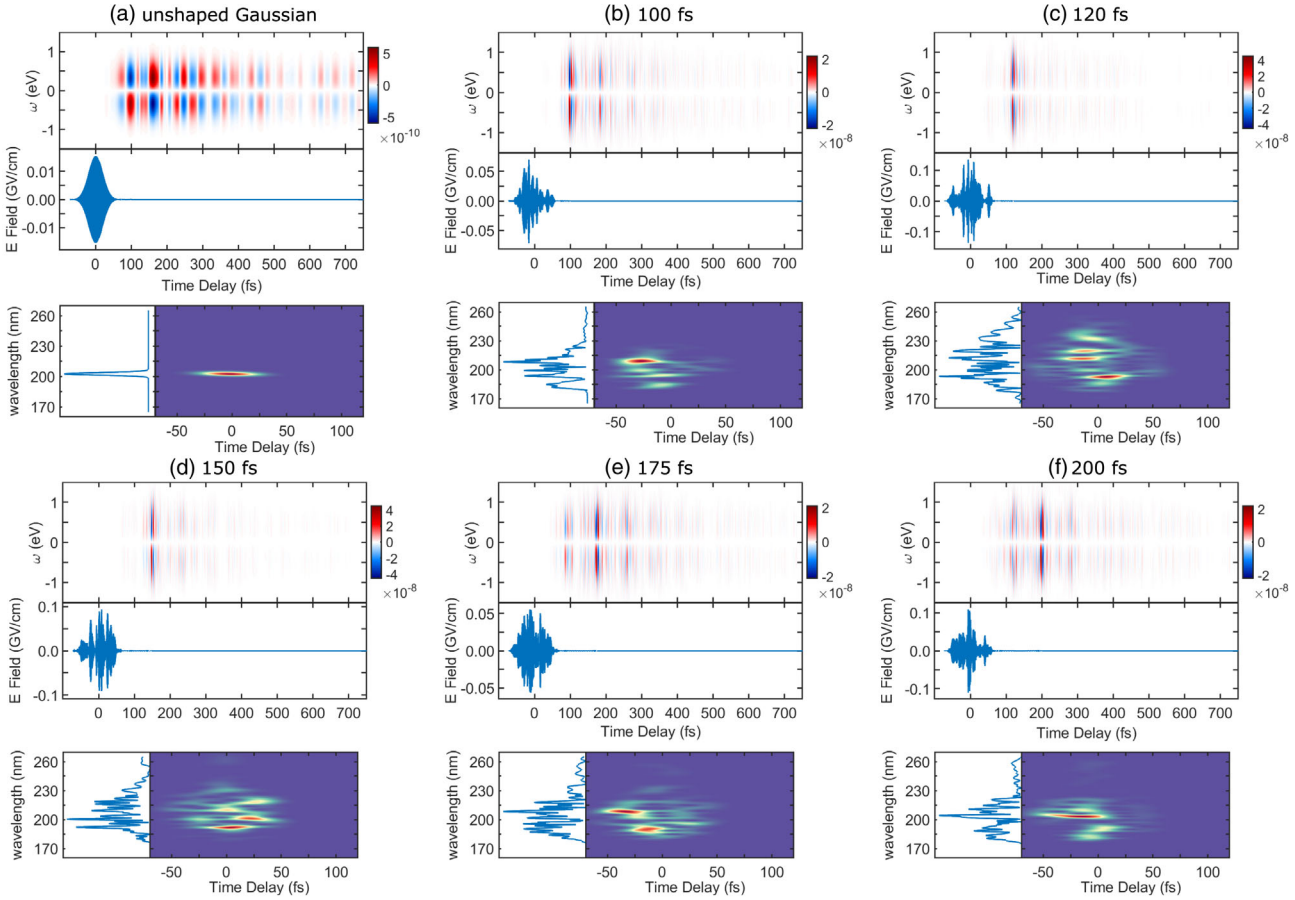

FIG. 3. Optimized laser pulses, spectrograms, and TRUECARS signals (a) before and (b)–(f) after pulse optimization by iterative solution of Eq. (2). The top panels contain the TRUECARS signal according to Eq. (1), the middle panels depict the laser fields ε_p that pump the system from S_0 to S_2, and the bottom panels show the pulse spectrograms calculated by Eq. (4). (a) Unoptimized, Gaussian-shaped pulse that has been used experimentally [27] and that serves as the guess field for OCT optimizations. (b)–(f) Optimized light fields for signal maximization at 100, 120, 150, 175, and 200 fs. Signal strengths are amplified by up to 200 orders of magnitude and precisely localized in time.

surface limits its precise controllability. At different times, the coherence magnitude is easier to maximize since the natural, uncontrolled wave packet motion is much closer than at other times. Second, $S_{\max}$ and $\langle\alpha\rangle_{\max}$ depend not only on the magnitude of the coherence, but also on its spatial position on the potential energy surface. This becomes evident by examining Fig. 1(c), where the polarizability is structured along the nuclear coordinates. Maximizing the coherence in a strong polarizability region yields larger $S_{\max}$ and $\langle\alpha\rangle_{\max}$, while maximizing it in regions of weaker polarizability decreases their maximum values.

TABLE I. Results of OCT optimizations. Starting from the unshaped 34 fs optical pump in Fig. 3(a), the control aim was to maximize $\langle\alpha_{xx}\rangle$ by iteratively solving Eq. (2). Five different final times T have been chosen, as indicated in the left column. $I_{\max}$ is the maximum pulse intensity, $\langle\alpha\rangle_{\max}$ is the expectation value of the transition polarizability, i.e., the control target, at this time and in atomic units, and $S_{\max}$ is the maximum value of the TRUECARS signal according to Eq. (1).

Target (fs)	$I_{\max}$ (W cm^{-2})	$\langle\alpha\rangle_{\max}$ (a.u.)	$S_{\max}$ (a.u.)
No OCT	3.15×10^{11}	1.72×10^{-6}	6.00×10^{-10}
100	6.81×10^{12}	1.53×10^{-5}	2.62×10^{-8}
120	2.44×10^{13}	2.41×10^{-5}	35.03×10^{-8}
150	1.15×10^{13}	2.80×10^{-5}	4.62×10^{-8}
175	4.16×10^{12}	1.52×10^{-5}	2.45×10^{-8}
200	1.61×10^{13}	1.74×10^{-5}	2.67×10^{-8}

The TRUECARS signal is defined as the time-integrated rate of change of photon numbers in the ε_0 field [19]

$$S(\omega) = \int dt \left\langle \frac{d\hat{N}^0_\omega}{dt} \right\rangle, \tag{5}$$

with the photon number operator $\hat{N}^0_\omega$. Increasing the signal strength by 2 orders of magnitude, as demonstrated here, thus means that around 100 times more photons contribute to the off-resonant stimulated Raman process and can be counted by the detector. This may be crucial for bringing

the TRUECARS signal, based on inherently weak vibronic coherences, above competing loss channels and thus allowing its detection.

Our control scheme based on Eq. (2) is applicable to other molecular systems and spectroscopic signals. Any signal that depends on the expectation value of a positive definite operator [33] can be optimized by replacing the polarizability with its time-dependent material quantity as the target in Eq. (2). A notable example is time-resolved x-ray diffraction [34,35]

$$S(q,T) = N \int dt |E(t-T)|^2 \langle \hat{\sigma}(-q,t)\hat{\sigma}(q,t)\rangle, \quad (6)$$

which depends on the molecular charge density $\sigma(q)$ in momentum space q or other instantaneous scattering-based measurements. The situation is more complicated for multidimensional signals that depend on multipoint correlation functions [36] of type

$$S(\omega,T) \propto \int dt \int d\tau \times \langle \psi(t_0)|U^\dagger(t,t_0)\hat{\mu}U(t,\tau)\hat{\mu}^\dagger U(\tau,t_0)|\psi(t_0), \quad (7)$$

including two time variables t and τ and a free propagation time $U(t,\tau)$ between the two field interactions. Adjusting the OCT formalism in Eq. (2) will be an interesting goal for a future study.

In optimal control experiments, pulse shaping is performed in the frequency domain by dispersing the laser pulse onto a liquid crystal spatial light modulator and modifying the different pixels to suppress specific frequencies [7,31]. The control problem is then solved iteratively by feeding the spectral output after sample interaction to an evolutionary algorithm and optimizing for a certain contribution. In the OCT presented here, shaping of the field is performed in the time domain, with the underlying control target given by a final quantum state of the molecular wave function, a quantity that is usually inaccessible to experiments. However, by formulating the control target in Eq. (2) in terms of a spectroscopic observable, we make it experimentally accessible.

In summary, we presented optimal control theory simulations that directly optimize for the TRUECARS signal that monitors vibronic coherences during conical intersection dynamics. The resulting conical intersection passage is then localized at a desired time and the signal is amplified by 2 orders of magnitude. Being intrinsically weak due to its dependence on decoherence caused by nuclear wave function overlap in different electronic states, this can be crucial for pushing the photon count in the signal above loss channels and allowing its detection. Our approach allows for optimization of virtually any spectroscopic observable that depends on molecular quantities expressed through the expectation value of a positive definite operator, given that there exists a solution on the molecular control landscape [37]. This procedure puts optimal control theory in closer connection to optimal control experiments that are similarly feedback driven by spectral signatures after interaction of the control field with the sample.

The data that support the findings of this study are available from the corresponding author upon reasonable request.

D. K. gratefully acknowledges support from the Alexander von Humboldt Foundation through the Feodor Lynen program. The support of the Chemical Sciences, Geosciences, and Biosciences division, Office of Basic Energy Sciences, Office of Science, U.S. Department of Energy through Award No. DE-FG02-04ER15571 and of the National Science Foundation (Grant No. CHE-1953045) is gratefully acknowledged. D. K. was partially supported by the DOE grant. We thank Markus Kowalewski for providing his QDng quantum dynamics code and Stefano Cavaletto for most valuable discussions.

*dkeefer@uci.edu
†smukamel@uci.edu

[1] S. J. Glaser, U. Boscain, T. Calarco, C. P. Koch, W. Köckenberger, R. Kosloff, I. Kuprov, B. Luy, S. Schirmer, T. Schulte-Herbrüggen, D. Sugny, and F. K. Wilhelm, Training Schrödinger's cat: quantum optimal control, Eur. Phys. J. D **69**, 279 (2015).
[2] H. Rabitz, R. de Vivie-Riedle, M. Motzkus, and K.-L. Kompa, Whither the future of controlling quantum phenomena? Science **288**, 824 (2000).
[3] W. Wohlleben, T. Buckup, J. L. Herek, and M. Motzkus, Coherent control for spectroscopy and manipulation of biological dynamics, Chem. Phys. Chem. **6**, 850 (2005).
[4] C. Consani, S. Ruetzel, P. Nuernberger, and T. Brixner, Quantum control spectroscopy of competing reaction pathways in a molecular switch, J. Phys. Chem. A **118**, 11364 (2014).
[5] J. Lim, C. M. Bösen, A. D. Somoza, C. P. Koch, M. B. Plenio, and S. F. Huelga, Multicolor Quantum Control for Suppressing Ground State Coherences in Two-Dimensional Electronic Spectroscopy, Phys. Rev. Lett. **123**, 233201 (2019).
[6] R. E. Goetz, A. Karamatskou, R. Santra, and C. P. Koch, Quantum optimal control of photoelectron spectra and angular distributions, Phys. Rev. A **93**, 013413 (2016).
[7] A. Assion, T. Baumert, M. Bergt, T. Brixner, B. Kiefer, V. Seyfried, M. Strehle, and G. Gerber, Control of chemical reactions by feedback-optimized phase-shaped femtosecond laser pulses, Science **282**, 919 (1998).
[8] J. L. Herek, W. Wohlleben, R. J. Cogdell, D. Zeidler, and M. Motzkus, Quantum control of energy flow in light harvesting, Nature (London) **417**, 533 (2002).
[9] M. Dantus and V. V. Lozovoy, Experimental coherent laser control of physicochemical processes, Chem. Rev. **104**, 1813 (2004).

[10] G. Vogt, G. Krampert, P. Niklaus, P. Nuernberger, and G. Gerber, Optimal Control of Photoisomerization, Phys. Rev. Lett. **94**, 068305 (2005).
[11] V. I. Prokhorenko, A. M. Nagy, S. A. Waschuk, L. S. Brown, R. R. Birge, and R. J. D. Miller, Coherent control of retinal isomerization in bacteriorhodopsin, Science **313**, 1257 (2006).
[12] C. M. Tesch and R. de Vivie-Riedle, Quantum Computation with Vibrationally Excited Molecules, Phys. Rev. Lett. **89**, 157901 (2002).
[13] C. Arenz and H. Rabitz, Controlling Qubit Networks in Polynomial Time, Phys. Rev. Lett. **120**, 220503 (2018).
[14] P. Rembold, N. Oshnik, M. M. Müller, S. Montangero, T. Calarco, and E. Neu, Introduction to quantum optimal control for quantum sensing with nitrogen-vacancy centers in diamond, AVS Quantum Sci. **2**, 024701 (2020).
[15] C. P. Koch, Controlling open quantum systems: tools, achievements, and limitations, J. Phys. Condens. Matter **28**, 213001 (2016).
[16] A. P. Peirce, M. A. Dahleh, and H. Rabitz, Optimal control of quantum-mechanical systems: Existence, numerical approximation, and applications, Phys. Rev. A **37**, 4950 (1988).
[17] D. J. Tannor and S. A. Rice, Control of selectivity of chemical reaction via control of wave packet evolution, J. Chem. Phys. **83**, 5013 (1985).
[18] R. Kosloff, S. Rice, P. Gaspard, S. Tersigni, and D. Tannor, Wavepacket dancing: Achieving chemical selectivity by shaping light pulses, Chem. Phys. **139**, 201 (1989).
[19] M. Kowalewski, K. Bennett, K. E. Dorfman, and S. Mukamel, Catching Conical Intersections in the Act: Monitoring Transient Electronic Coherences by Attosecond Stimulated X-Ray Raman Signals, Phys. Rev. Lett. **115**, 193003 (2015).
[20] D. Keefer, T. Schnappinger, R. de Vivie-Riedle, and S. Mukamel, Visualizing conical intersection passages via vibronic coherence maps generated by stimulated ultrafast X-ray Raman signals, Proc. Natl. Acad. Sci. U.S.A. **117**, 24069 (2020).
[21] S. M. Cavaletto, D. Keefer, and S. Mukamel, High Temporal and Spectral Resolution of Stimulated X-Ray Raman Signals with Stochastic Free-Electron-Laser Pulses, Phys. Rev. X **11**, 011029 (2021).
[22] J. Somlói, V. A. Kazakov, and D. J. Tannor, Controlled dissociation of I2 via optical transitions between the X and B electronic states, Chem. Phys. **172**, 85 (1993).
[23] C. Gollub, M. Kowalewski, and R. de Vivie-Riedle, Monotonic Convergent Optimal Control Theory with Strict Limitations on the Spectrum of Optimized Laser Fields, Phys. Rev. Lett. **101**, 073002 (2008).
[24] P. von den Hoff, S. Thallmair, M. Kowalewski, R. Siemering, and R. de Vivie-Riedle, Optimal control theory – closing the gap between theory and experiment, Phys. Chem. Chem. Phys. **14**, 14460 (2012).
[25] D. Keefer, S. Thallmair, S. Matsika, and R. de Vivie-Riedle, Controlling photorelaxation in uracil with shaped laser pulses: A theoretical assessment, J. Am. Chem. Soc. **139**, 5061 (2017).
[26] W. Zhu and H. Rabitz, A rapid monotonically convergent iteration algorithm for quantum optimal control over the expectation value of a positive definite operator, J. Chem. Phys. **109**, 385 (1998).
[27] S. Matsika, M. Spanner, M. Kotur, and T. C. Weinacht, Ultrafast relaxation dynamics of uracil probed via strong field dissociative ionization, J. Phys. Chem. A **117**, 12796 (2013).
[28] *Non-Linear Raman Spectroscopy and Its Chemical Aplications*, edited by W. Kiefer and D. A. Long (Springer, Dordrecht, Netherlands, 1982).
[29] J. Olsen and P. Jørgensen, Linear and nonlinear response functions for an exact state and for an MCSCF state, J. Chem. Phys. **82**, 3235 (1985).
[30] R. Trebino, K. W. DeLong, D. N. Fittinghoff, J. N. Sweetser, M. A. Krumbügel, B. A. Richman, and D. J. Kane, Measuring ultrashort laser pulses in the time-frequency domain using frequency-resolved optical gating, Rev. Sci. Instrum. **68**, 3277 (1997).
[31] A. Weiner, D. Leaird, J. Patel, and J. Wullert, Programmable shaping of femtosecond optical pulses by use of 128-element liquid crystal phase modulator, IEEE J. Quantum Electron. **28**, 908 (1992).
[32] J. Köhler, M. Wollenhaupt, T. Bayer, C. Sarpe, and T. Baumert, Zeptosecond precision pulse shaping, Opt. Express **19**, 11638 (2011).
[33] S. Mukamel, *Principles of Nonlinear Optics and Spectroscopy* (Oxford University Press, New York, 1995).
[34] K. Bennett, M. Kowalewski, J. R. Rouxel, and S. Mukamel, Monitoring molecular nonadiabatic dynamics with femtosecond X-ray diffraction, Proc. Natl. Acad. Sci. U.S.A. **115**, 6538 (2018).
[35] D. Keefer, F. Aleotti, J. R. Rouxel, F. Segatta, B. Gu, A. Nenov, M. Garavelli, and S. Mukamel, Imaging conical intersection dynamics during azobenzene photoisomerization by ultrafast X-ray diffraction, Proc. Natl. Acad. Sci. U.S.A. **118**, e2022037118 (2021).
[36] M. Kowalewski, B. P. Fingerhut, K. E. Dorfman, K. Bennett, and S. Mukamel, Simulating coherent multidimensional spectroscopy of nonadiabatic molecular processes: from the infrared to the x-ray regime, Chem. Rev. **117**, 12165 (2017).
[37] B. Russell, H. Rabitz, and R.-B. Wu, Control landscapes are almost always trap free: A geometric assessment, J. Phys. A **50**, 205302 (2017).